## PAPER

# Multi-stimulus linear negative expansion of a breathing M(O₂CR)₄-node MOF†

Daniel Watkins,[a] Thomas M. Roseveare, [iD][a] Mark R. Warren,[b]
Stephen P. Thompson,[b] Ashleigh J. Fletcher [iD][c] and Lee Brammer [iD] *[a]

The metal–organic framework $(Me_2NH_2)_2[Cd(NO_2BDC)_2]$ (**SHF-81**) comprises flattened tetrahedral $Cd(O_2CR)_4^{2-}$ nodes, in which Cd(II) centres are linked via $NO_2BDC^{2-}$ ligands (2-nitrobenzene-1,4-dicarboxylate) to give a doubly interpenetrated anionic network, with charge balanced by two $Me_2NH_2^+$ cations per Cd centre resident in the pores. The study establishes that this is a twinned α-quartz-type structure (trigonal, space group $P3_x21$, $x = 1$ or 2), although very close to the higher symmetry β-quartz arrangement (hexagonal, $P6_x22$, $x = 2$ or 4) in its as-synthesised solvated form $[Cd(NO_2BDC)_2] \cdot 2DMF \cdot 0.5H_2O$ (**SHF-81-DMF**). The activated MOF exhibits very little $N_2$ uptake at 77 K, but shows significant $CO_2$ uptake at 273–298 K with an isosteric enthalpy of adsorption ($\Delta H_{ads}$) at zero coverage of $-27.4$ kJ $mol^{-1}$ determined for the MOF directly activated from **SHF-81-DMF**. A series of in situ diffraction experiments, both single-crystal X-ray diffraction (SCXRD) and powder X-ray diffraction (PXRD), reveal that the MOF is flexible and exhibits breathing behaviour with observed changes as large as 12% in the a- and b-axes ($|\Delta a|$, $|\Delta b| < 1.8$ Å) and 5.5% in the c-axis ($|\Delta c| < 0.7$ Å). Both the solvated **SHF-81-DMF** and activated/desolvated **SHF-81** forms of the MOF exhibit linear negative thermal expansion (NTE), in which pores that run parallel to the c-axis expand in diameter (a- and b-axis) while contracting in length (c-axis) upon increasing temperature. Adsorption of $CO_2$ gas at 298 K also results in linear negative expansion ($\Delta a$, $\Delta b > 0$; $\Delta c < 0$; $\Delta V > 0$). The largest change in dimensions is observed during activation/desolvation from **SHF-81-DMF** to **SHF-81** ($\Delta a$, $\Delta b < 0$; $\Delta c > 0$; $\Delta V < 0$). Collectively the nine in situ diffraction experiments conducted suggest the breathing behaviour is continuous, although individual desolvation and adsorption experiments do not rule out the possibility of a gating or step at intermediate geometries that is coupled with continuous dynamic behaviour towards the extremities of the breathing amplitude.

[a]Department of Chemistry, University of Sheffield, Brook Hill, Sheffield S3 7HF, UK. E-mail: lee.brammer@
sheffield.ac.uk
[b]Diamond Light Source, Harwell Science and Innovation Campus, Didcot, Oxon, OX11 0DE, UK
[c]Department of Chemical and Process Engineering, University of Strathclyde, 75 Montrose Street, Glasgow G1
1XJ, UK

† Electronic supplementary information (ESI) available: Further details on all experimental studies can be found in the supporting information, including synthesis and characterisation, and all SCXRD and PXRD studies. CCDC 2013011–2013023. For ESI and crystallographic data in CIF or other electronic format see DOI: 10.1039/d0fd00089b

# Introduction

Extensive interest in metal–organic frameworks (MOFs) over the past two decades has centred on their modular design and the wide range of applications that exploit their molecular-scale porosity, including selective gas adsorption/separation,[1–3] catalysis,[4–6] energy storage and conversion,[7] sensing,[8,9] and drug delivery. Most reported MOFs are ostensibly rigid materials, which possess empty pores or channels that, after activation, can be used to encapsulate small-molecule guests under certain conditions. There are, however, a growing number of MOFs that exhibit often reversible flexible behaviour in response to external stimuli. There is much interest in understanding this behaviour and in the development of applications related to the differential responses to changes in stimuli such as guest inclusion, light, temperature or pressure.[10–16] In particular, so-called "breathing" behaviour, in which framework flexibility enables the reversible contraction and expansion of pores, is very attractive due to the potential for selective guest inclusion, for example in the field of gas separation,[17] but also increasingly in other areas such as catalysis,[18] modulation of photophysical behaviour,[19] or energy storage and mechanical response.[20,21]

Almost all "breathing" MOFs are reported to exist in two or more discrete states with different pore dimensions, at least a narrow-pore and a wide-pore (open and closed) form. Such MOFs include the archetypical MIL-53 family[22] and those based on DMOF,[23] and can involve multiple intermediate states, such as in the case of Co(bdp)[24] (bdp = benzenedipyrazolate). In the examples noted, flexibility arises from hinge-like deformations in metal–ligand coordination, and often leads to gated adsorption of gases, although in other framework materials gating can arise from the deformation of flexible ligands.[25] In contrast to the growing number of published MOFs that exhibit the aforementioned discrete flexibility, there are very few materials that have been shown to exhibit continuous dynamic behaviour. Examples include the MIL-88 family,[26] which display this property under solvent uptake, and SHF-61, which displays a continuous pore-closing mechanism during activation to remove DMF.[27]

A growing area of interest in the context of cooperative phenomena in framework materials is the anomalous mechanical response associated with phenomena such as negative thermal expansion (NTE),[28] negative linear compressibility (NLC)[29] and auxetic behaviour,[30] which have been concisely introduced by Goodwin and colleagues (Fig. 1),[31] and have potential for applications in composite materials with thermally adjustable expansion (NTE) or pressure sensors (NLC and auxetic materials). In their report, Goodwin and co-workers undertook neutron powder diffraction (NPD) studies over a wide temperature range for two perdeuterated quartz-like MOFs after prior activation.[31] These studies illustrated uniaxial NTE behaviour for $D[In(BDC-d_4)_2]$ and uniaxial positive thermal expansion (PTE) for $[Zn(isonicotinate)_2]$, and geometric criteria were developed for the prediction of these behaviours in other related MOFs.

Here we report a new example of continuous breathing and uniaxial expansion/contraction behaviour in the MOF $(Me_2NH_2)_2[Cd(NO_2BDC)_2]\cdot 2DMF\cdot0.5H_2O$ (**SHF-81-DMF**) ($NO_2BDC^{2-}$, 2-nitrobenzene-1,4-dicarboxylate (2-nitroterephthalate); SHF, Sheffield Framework), for which this anisotropic flexible response can be accessed by different stimuli. Specifically, we describe the
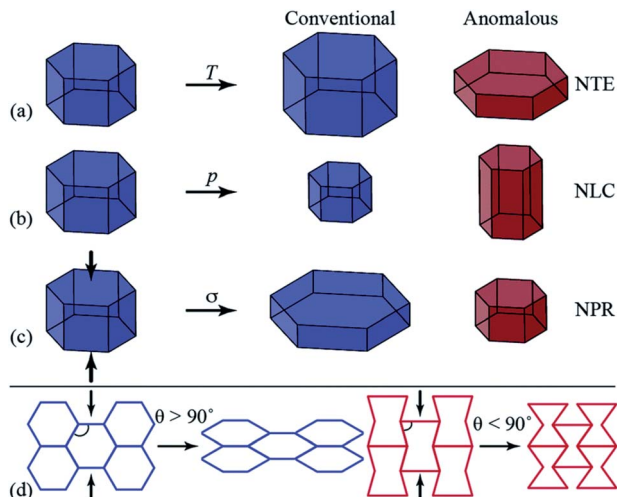
Fig. 1 Diagrammatic representation of anomalous mechanics for materials exhibiting (a) uniaxial negative thermal expansion (NTE), contraction in one direction upon heating ($T$); (b) negative linear compressibility (NLC), expansion in one direction under hydrostatic pressure ($p$); and (c) auxetic response upon axial compression ($\sigma$, indicated by the arrows), whereby a negative Poisson's ratio (NPR) is observed. (d) Honeycomb frameworks with different geometries (framework angle, $\theta$) exhibit contrasting mechanical responses to axial compression. Reproduced from ref. 31 with permission of The Royal Society of Chemistry.

dynamic framework responses to stimulation by activation (solvent loss), gas adsorption or change in temperature. Structural insight into the flexible behaviour is provided by extensive single-crystal and powder X-ray diffraction studies. Originally reported as a static MOF,[32] we demonstrate that this material is unusual, not only in its dynamic behaviour, but in that this behaviour can be documented by single-crystal X-ray diffraction. **SHF-81-DMF** comprises two identical interpenetrated networks of qtz topology (*i.e.* based on the quartz network). The networks are constructed from $Cd^{2+}$ ions, which serve as distorted tetrahedral $Cd(O_2CR)_4^{2-}$ nodes, connected *via* nitroterephthalate linkers that coordinate the metal centres in a chelating manner. The anionic framework contains charge-balancing dimethylammonium cations, DMF and water molecules in its triangular channels.

## Experimental

### General

Reagents and solvents were obtained from Sigma-Aldrich, Alfa Aesar, Acros Organics, Fisher Scientific, Fluorochem or Manchester Organics, and were used without additional purification. Samples used for elemental analysis, thermogravimetric analysis and laboratory powder X-ray diffraction were ground into a powder using a mortar and pestle immediately prior to analysis, to ensure consistency of solvent content in the bulk material. For solution-phase NMR spectroscopic characterisation, the sample (*ca.* 3 mg) was acid-digested in 50 µL

deuterium chloride (35% in $D_2O$) in 1 mL DMSO-$d_6$. Thermogravimetric analysis was performed in air using a PerkinElmer Pyris1 Thermogravimetric Analyser. Elemental analysis was performed by combustion in pure oxygen using a Perki-nElmer 2400 CHNS/O Series II Analyser or an Elementar Vario MICRO cube analyser. NMR spectroscopy (400 MHz) was performed using Bruker AVANCE III 400 HD or AVANCE 400 HD spectrometers.

### Synthesis

Cadmium nitrate hexahydrate (0.3072 g, 0.993 mmol), 2-nitroterephthalic acid (0.4210 g, 1.994 mmol), dimethylamine hydrochloride (8.0 mg, 98 µmol) and $N,N$-dimethylformamide (DMF) (10 mL) were stirred for *ca.* 5 min (until dissolution of the solids) in a 23 mL Teflon vessel. The Teflon vessel was then sealed inside a stainless steel autoclave, heated to 130 °C at a rate of 1 °C min$^{-1}$ and held at 130 °C for 24 h. The vessel was then cooled to room temperature at a rate of 0.1 °C min$^{-1}$ and the product (orange crystalline needles; 0.5621 g, 0.738 mmol, 74%) was washed with DMF and stored under DMF. Found: C, 40.16%; H, 4.74%; N, 10.74%. Expected: C, 40.14%; H, 4.79%; N, 10.80%. Yield and expected elemental analysis calculated using the formula: $[Me_2NH_2]_2[Cd(NO_2BDC)_2]\cdot$ $2DMF\cdot0.5H_2O$. Phase purity of the sample was confirmed by Pawley fitting of PXRD data (Fig. S5†). Further details of characterisation by TGA and by solution-phase NMR spectroscopy following acid digestion are provided in the ESI.†

### Gas adsorption

Gravimetric $CO_2$ adsorption measurements were made using an Intelligent Gravimetric Analyser (IGA-003) supplied by Hiden Isochema Ltd, which was thermally regulated *via* active computer control. A computer algorithm was applied to monitor the approach to equilibrium at each pressure step. Prior to measurements, the sample was activated at room temperature under ultra-high vacuum ($10^{-8}$ bar) until constant mass was attained. Adsorption isotherms for $CO_2$ were measured at 273, 288 and 298 K and used to determine the isosteric enthalpy of adsorption (see Fig. S11 and S12†). Volumetric $N_2$ adsorption was performed on a Micromeritics ASAP 2020Plus Analyser. The sample (*ca.* 100 mg) was desolvated at 80 °C under vacuum overnight (*ca.* 16 hours) using standard Schlenk techniques, transferred to the analyser and degassed for a further 16 hours under vacuum at 80 °C prior to analysis. Nitrogen uptake was performed at 77 K using a liquid $N_2$ bath for temperature control (Fig. S10†).

### Powder X-ray diffraction

Laboratory powder X-ray diffraction (PXRD) experiments were performed using a Bruker D8 Advance diffractometer equipped with Göbel mirrors, and recorded in the range $3° < 2\theta < 60°$ using Cu-K$_\alpha$ radiation. Data collection was performed with Debye–Scherrer geometry, with a rotating capillary stage. Samples were loaded in 0.7 mm borosilicate capillaries. Temperature was either ambient (routine collections), or controlled using an Oxford Cryosystems Cryostream Plus device. Synchrotron powder X-ray diffraction data were collected at Beamline I11, Diamond Light Source using a wide-angle position-sensitive detector comprising 18 Mython-2 modules.[33,34] Samples were packed into 0.7 mm quartz capillaries built into a gas cell to allow sample evacuation and $CO_2$ uptake. A pair of scans

was collected for each measurement, related by a 0.25° detector offset, to account for gaps between modules. At each gas pressure four such pairs of patterns were summed to give the final pattern used for analysis. All powder diffraction data were analysed by Pawley refinement,[35] using TOPAS 4.1.[36]

### Single-crystal X-ray diffraction

Laboratory single-crystal X-ray diffraction (SCXRD) experiments were performed using either a Bruker APEX-II CCD diffractometer with 3-circle SMART or 4-circle KAPPA platform and a Mo-K$_\alpha$ sealed-tube X-ray source, or a Bruker D8 Venture diffractometer with a PHOTON 100 dual-CMOS chip detector, operating with a Cu-K$_\alpha$ I$\mu$S microfocus X-ray source. Data were processed using the *APEX-3* suite of programs.[37] Sample temperature was maintained using an Oxford Cryosystems Cryostream 700 or CryostreamPlus 700 device. Samples were mounted directly from the mother liquor, unless stated otherwise. Absorption correction was performed using empirical methods (*SADABS*) based on symmetry-equivalent reflections combined with measurements at different azimuthal angles.[38] Synchrotron SCXRD data were recorded at Beamline I19, Diamond Light Source. The crystal was carefully glued to a Mylar loop, ensuring minimum coverage of the crystal with glue, and loaded into a 1.0 mm quartz capillary built into a gas cell to allow CO$_2$ uptake. A minimum of one hemisphere of data was collected using three 132° and one 180° omega scans, with 0.4° slicing, on a Newport diffractometer using a Pilatus 300 K detector.[39] Data processing and absorption correction was performed using Rigaku Oxford Diffraction *CrysalisPro*.[40] Crystal structures were solved and refined against $F^2$ values the program *SHELXL*[41] implemented *via* OLEX-2.[42] All non-hydrogen atoms were refined anisotropically except for some of the structures in which positional disorder of the cations or orientational disorder of the linker ligand was required. Crystallographic restraints and constraints were applied to some structures where necessary. Positions of hydrogen atoms were calculated with idealised geometries and refined using a riding model with isotropic displacement parameters. The *PLATON* function *SQUEEZE*[43] was applied in some cases to determine the contribution to the structure factors of the unmodelled electron density of solvent molecules and/or the cations in the MOF pores, where otherwise poor convergence of the least-squares refinement resulted.

## Results & discussion

### Synthesis, crystal structure & bulk-phase characterisation

[Me$_2$NH$_2$]$_2$[Cd(NO$_2$BDC)$_2$]·2DMF·0.5H$_2$O (**SHF-81-DMF**) was prepared by a modification of the reported solvothermal procedure,[32] which, in our hands, had yielded no product. Our procedure uses a different stoichiometry of reactants, milder conditions and a considerably shorter reaction time, and is further facilitated by adding to the reaction mixture 0.05 equivalents of [Me$_2$NH$_2$]Cl, which may have a templating effect, enabling a 74% yield. The majority of NMe$_2$H$_2^+$ cations present in the crystalline product, however, result from *in situ* hydrolysis of DMF. We note that precise control of the water content in the reaction mixture was not attempted. The composition and phase purity of the product were established by a combination of elemental analysis, thermogravimetric analysis

(Fig. S4†), $^1H$ and $^{13}C$ NMR spectroscopy of acid-digested material (Fig. S1–S3†) and PXRD (Fig. S5†); the crystal structure was determined by SCXRD. The composition of the solvated form of the MOF (**SHF-81-DMF**) is presented henceforth as $[Me_2NH_2]_2[Cd(NO_2BDC)_2]\cdot 2DMF\cdot 0.5H_2O$, which closely approximates consistent compositions determined by the aforementioned range of characterisation techniques.

The crystal structure of **SHF-81-DMF** (Fig. 2) consists of a doubly interpenetrated qtz network constructed from 8-coordinate cadmium(II) ions, which serve as network nodes, each chelated by four nitroterephthalate ($NO_2BDC^{2-}$)



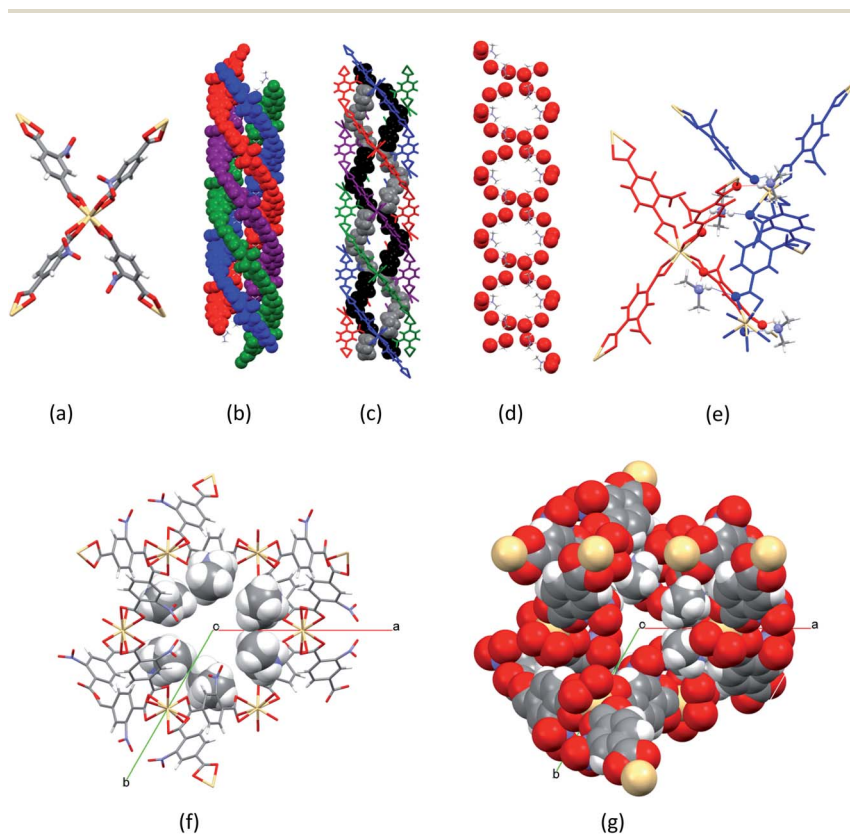Fig. 2 Crystal structure of doubly-interpenetrated $[Me_2NH_2]_2[Cd(NO_2BDC)_2]\cdot 2DMF\cdot 0.5H_2O$ (**SHF-81-DMF**) framework structure at 100 K, showing (a) $Cd(O_2CR)_4{}^{2-}$ node; (b) quadruple helix arrangement of the framework along the c-axis (vertical) (blue and purple helices are part of one network; red and green helices are part of the other network); (c) quadruple helix arrangement of the framework, showing the double helix arrangement of the $Me_2NH_2{}^+$ cations (black and grey) in the channels; (d) double helix arrangement of $Me_2NH_2{}^+$ cations along the c-axis, emphasising framework carboxylate oxygens (red) which accept N–H⋯O hydrogen bonds from the cations and adopt a double-helix arrangement to match that of the cations; (e) N–H⋯O hydrogen bonds from the cations linking two networks, shown in red and blue (N, H and O atoms are emphasised); (f) view down the c-axis of a triangular channel, showing inwardly oriented nitro groups and the location of cations (shown in space-filling representation); (g) view down the c-axis of a triangular channel (all atoms in space-filling representation). Atom colours for parts (a), (d), (f) and (g): Cd, beige; O, red; N, blue; C, grey; H, white.

linkers to give a flattened pseudo-tetrahedral node geometry (Fig. 2a). The two networks give rise to a quadruple helix arrangement along the $c$-axis, in which every second helix component is connected to the same network (Fig. 2b). Triangular channels run parallel to the $c$-axis and are lined by inwardly oriented nitro groups (Fig. 2f and g). Within these channels the $Me_2NH_2^+$ cations are arranged in a double helix arrangement of opposite handedness to the framework helices, each cation forming N–H⋯O hydrogen bonds to carboxylate oxygens associated with two $Cd(O_2CR)_4^{2-}$ nodes (Fig. 2c–e). The channels are further occupied by DMF and water molecules, established from bulk-phase characterisation but not modelled crystallographically.

The crystal structure is modelled as a merohedral twin in trigonal space group $P3_x21$ ($x = 1$ or 2; crystals of each enantiomorph are present in any given batch). Twinning occurs *via* a 2-fold rotation about the $c$-axis, with the contribution of the twin domains refining to 0.51(1) : 0.49(1). This is an analogous description to that of Dauphiné twins in α-quartz,[44] which adopts the same trigonal space group(s). It is also possible to refine a structural model for **SHF-81-DMF** in hexagonal space group $P6_x22$ ($x = 2$ or 4; crystals of each enantiomorph are present in any given batch), the space group adopted by β-quartz[44] and reported for the analogous MOF QMOF-2 (*vide supra*),[45] but this model gives poorer indices of fit ($R1$, $wR2$, $R_{int}$) and has a number of other unsatisfactory features. The hexagonal model requires two-fold rotational disorder of the nitroaromatic moieties ($C_6H_3NO_2$), which in the simplest model can be described in terms of disorder of the nitro group across two adjacent ring positions; cations or solvent molecules could not be modelled. The twinned trigonal model, in contrast, does not require this disorder to be invoked for the nitro substituents and allows modelling of the ordered network of cations that shows the hydrogen bonding arrangement along the channels (Fig. 2c–e). The previous report of the crystal structure used a model in hexagonal space group $P6_222$ and suffers the same deficiencies as our refinements in the space group.[32] The necessity of the twinned trigonal model becomes more apparent upon desolvation of the MOF to generate **SHF-81**, for which a hexagonal model no longer provides an approximate fit (*vide infra*). Thus, **SHF-81** adopts a Dauphiné twin α-quartz structure, whereas **SHF-81-DMF** adopts the same type of structure, but one that lies much closer to the β-quartz structure.

### Activation studies: discovery of flexible behaviour

The TGA studies of **SHF-81-DMF** are consistent with stepwise removal of solvent from 80–130 °C, followed by cation degradation *via* loss of $Me_2NH$ at 230–280 °C, behaviour that compares well with that previously reported for the MOF SHF-61-DMF $[Me_2NH_2][In(NH_2BDC)_2]\cdot1.75DMF\cdot1.25H_2O$.[27] Heating a sample of **SHF-81-DMF** in powder form at 80 °C under dynamic vacuum for 16 h resulted in desolvation, but retention of the $Me_2NH_2^+$ cations, yielding $[Me_2NH_2]_2[Cd(NO_2BDC)_2]$ (**SHF-81**), as indicated by ^{1}H NMR spectroscopy following acid digestion (Fig. S6†). PXRD data show that the material is still a single phase; the Pawley fits indicate substantial changes in unit cell dimensions determined at 295 K (Table 1; **SHF-81-DMF**, Fig. S5;† **SHF-81**, Fig. S7†) and suggest anisotropic breathing behaviour that involves contraction of the framework along the equivalent $a$- and $b$-axes, but expansion along the $c$-axis. A breathing response of similar magnitude was also achieved in single crystals of **SHF-81-DMF** by heating

**Table 1** Unit cell parameters for solvated **SHF-81-DMF** and activated/desolvated **SHF-81**

| Technique | Temperature | | $a$/Å | $c$/Å | $V$/Å³ |
|---|---|---|---|---|---|
| SCXRD[a] | 100 K | **SHF-81-DMF** | 14.8922(7) | 12.7663(6) | 2452.0(3) |
| | | **SHF-81** | 13.619(1) | 13.229(1) | 2124.9(5) |
| | 195 K | **SHF-81-DMF** | 15.0467(5) | 12.6619(4) | 2482.6(2) |
| | | **SHF-81** | 13.7702(3) | 13.2048(3) | 2168.4(1) |
| PXRD[b] | 298 K | **SHF-81-DMF** | 15.3550(3) | 12.5133(4) | 2555.1(1) |
| | | **SHF-81** | 13.931(2) | 13.148(3) | 2209.6(9) |

[a] Data for solvated **SHF-81-DMF** were collected on crystals that adopted space group $P3_221$; data for desolvated **SHF-81** were collected on separate crystals that adopted space group $P3_121$. [b] Pawley refinements using space group $P3_121$.

on a glass slide in a temperature-controlled oven at 100 °C for 1 h. SCXRD data were collected at 100 K and 195 K and used in crystal structure refinements for **SHF-81** (Table 1). Comparisons of unit cell data across the three temperatures, in either the solvated or activated/desolvated state, also indicate an anisotropic thermal expansion, consistent with the dynamic framework behaviour associated with activation and with the linear NTE behaviour of the analogous MOF QMOF-2,[45] reported as D[In(BDC-d$_4$)$_2$].[31]

The change in the unit cell parameters upon activation of the MOF is consistent with narrowing and lengthening of the channels in the material, which run parallel to the $c$-axis (Fig. 2). The flexibility of the framework can be viewed at a local level in terms of the hinge-like motion of the nitroterephthalate ligands (NO$_2$BDC$^{2-}$) described in terms of rotation of the ligand about the O···O vector of its carboxylate groups (Fig. 3). The crystal structures contain one independent ligand with two crystallographically distinct carboxylate groups. Upon desolvation,‡ the hinge angle at the carboxylate group *ortho* to the nitro substituent increases from 167.5° to 178.1°, whereas at the other carboxylate group the hinge angle decreases from 173.9° to 162.0°; the Cd···Cd distance is reduced by only approx. 0.14 Å (11.3084(4) to 11.1662(8) Å). The magnitudes of the changes are similar to those of the flexible diamondoid MOF SHF-61,[27] which is based on distorted tetrahedral In(O$_2$CR)$_4^-$ nodes linked by aminoterephthalate ligands.

The flexibility of the framework and its relationship to the changes in unit cell dimensions can be seen more readily by consideration of the framework angles defined by Cd nodes (Cd···Cd···Cd). The crystal structures contain one crystallographically unique Cd centre, which resides on a 2-fold rotation axis in the $P3_x21$ space group. There are two unique alternating Cd···Cd···Cd angles ($\varphi_1$, $\varphi_2$) that propagate the helical chains, with each turn of the helix comprising six Cd(II) centres and six NO$_2$BDC$^{2-}$ ligands (Fig. 4 and Fig. S8†). In the hexagonal β-quartz structure $\varphi_1 = \varphi_2$, but in the lower symmetry α-quartz structure $\varphi_1 \neq \varphi_2$. In **SHF-81-DMF** $\varphi_1 = 141.48°$ and $\varphi_2 = 141.63°$, confirming that the structure is close to the β-quartz type, but upon desolvation/activation the angles change to $\varphi_1 = 151.27°$ and $\varphi_2 = 137.59°$, which very clearly indicates an α-quartz type structure. This change lengthens the helix pitch from 51.065(3) to 52.912(5) Å (4 × $c$-axis

‡ Distances and angles used in the section to quantify changes in crystal structure upon desolvation/activation are those for the crystal structures of **SHF-81-DMF** and **SHF-81** at 100 K.
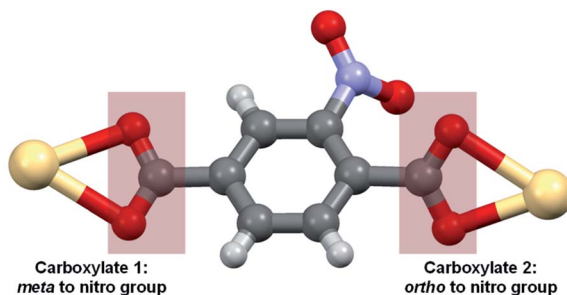
| MOF | M···M (Å) | Hinge-angle 1 (°) | Hinge-angle 2 (°) |
|---|---|---|---|
| SHF-81-DMF | 11.308 | 173.9 | 167.5 |
| SHF-81 | 11.166 | 162.0 | 178.1 |
| SHF-61-DMF[a] | 11.009 | 163.7 | 165.4 |
| SHF-61[a] | 10.908 | 175.8 | 174.8 |

[a] Data from ref. 27

Fig. 3 Carboxylate coordination for $NO_2BDC^{2-}$ to consecutive Cd centres in the framework **SHF-81**. Analogous coordination is found for $NH_2BDC^{2-}$ to consecutive In centres in the framework SHF-61. Tabulated hinge angles at the two carboxylate groups (*meta* and *ortho* to the ring substituent) are defined as the angle M···(OO centroid)···($C_6$ ring centroid). Where disorder of the carboxylate group has been modelled, the angles refer to the major component of the model. All single-crystal structures at 100 K (except SHF-61 at 105 K).

length) and results in three of the six Cd(II) centres in each helical turn moving towards the centre of a given channel and three moving away, in an alternating pattern (Fig. 4c and d). Of the six Cd···Cd···Cd angles that can be defined around each tetrahedral network node associated with a Cd(II) centre (Fig. S8†), local 2-fold rotational symmetry requires that four are unique. The remaining two unique angles change from $\varphi_3 = 82.36°$ and $\varphi_4 = 110.47°$ in **SHF-81-DMF** to $\varphi_3 = 75.15°$ and $\varphi_4 = 115.83°$ in **SHF-81**. The changes in Cd···Cd···Cd angles upon activation/desolvation are also reflected in changes in the distances between consecutive nitro groups along each chain. As measured by the N···N separations, these change from 7.153 and 11.662 Å in **SHF-81-DMF** to 8.699 and 10.821 Å in **SHF-81** (distances for major components of the rotationally disordered nitroaromatic group in **SHF-81** are listed).

### *In situ* diffraction studies of framework dynamic response to multiple stimuli: activation, $CO_2$ adsorption and temperature

In order to explore the initial findings, *in situ* diffraction studies were conducted to examine the response of the framework to different stimuli in more detail. We examined (i) activation of **SHF-81-DMF** and the dynamic structural response to pore-solvent removal, (ii) adsorption of $CO_2$ gas by activated **SHF-81** and the resultant dynamic framework response, and (iii) the uniaxial NTE response to change of temperature in both **SHF-81-DMF** and its activated/desolvated counterpart **SHF-81**.

(a)

51.065(3) Å

$\Phi_1$ (Cd···Cd···Cd)
= 141.48 °

$\Phi_2$ (Cd···Cd···Cd)
= 141.63 °

(b)

(c)

52.912(5) Å

$\Phi_1$ (Cd···Cd···Cd)
= 151.27 °

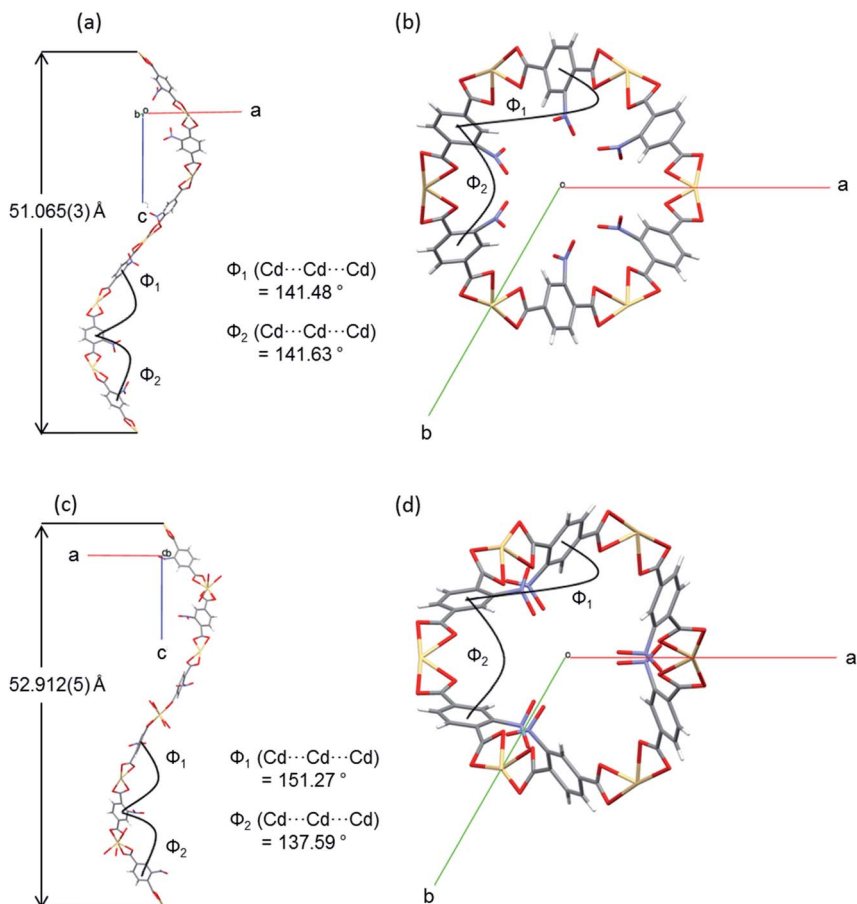$\Phi_2$ (Cd···Cd···Cd)
= 137.59 °

(d)

**Fig. 4** A single turn of a helix viewed perpendicular and parallel to the $c$-axis, along which the helices and accompanying pores propagate, shown with dimensions for alternating Cd···Cd···Cd angles ($\varphi_1$, $\varphi_2$) and the helix pitch, for (a) and (b) **SHF-81-DMF**; (c) and (d) **SHF-81**. Single-crystal structures determined at 100 K.

**Activation of SHF-81-DMF.** Sequences of SCXRD and PXRD experiments were conducted to monitor the changes in structure of the framework of **SHF-81-DMF** upon heating to remove the pore solvent. In each case the sample (single crystal on a MiTeGen mount or powder in a capillary) was heated to a specified temperature for 30 min then returned to 298 K and allowed to equilibrate for 5 min before measurement either of diffraction intensities on a fixed number of frames (SCXRD) or of a powder pattern, which were then indexed and used to determine the unit cell dimensions by standard least-squares methods. Each study comprised a series of sequential measurements conducted in this manner after heating at progressively higher temperatures, ranging from 298 K to 433 K.

In both studies, progressive heating at higher temperatures results in gradual contraction of the equivalent $a$- and $b$-axes and expansion of the $c$-axis, *i.e.* area negative expansion, leading to a gradual reduction in unit cell volume (Fig. 5). The sequence of lattice parameters determined suggests a continuous breathing
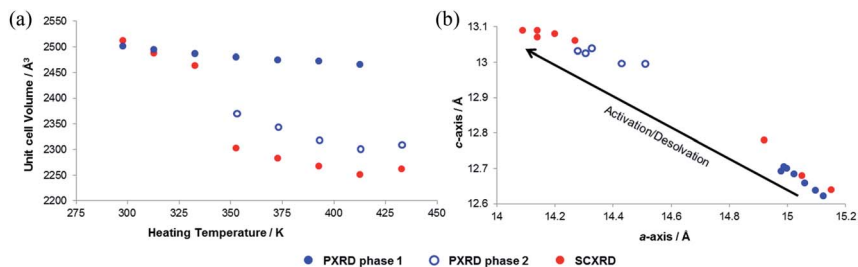
Fig. 5 Progressive changes (a) in unit cell volume (determined at 298 K) as a sequential function of heating temperature, and (b) in lattice parameters during activation/desolvation of **SHF-81-DMF** from *in situ* SCXRD and PXRD studies.

behaviour, although it is noted that a more substantial change occurs for both studies between the measurement following heating at 333 K and that following heating at 353 K. For the SCXRD study, there is a substantial change in the unit cell of the crystal studied at this point (Table S3†), whereas for the PXRD study initially only a small fraction of the sample undergoes this change (Fig. S9 and Table S4†). Thus, after heating the powder sample to 333 K, two phases of the MOF are required for a satisfactory Pawley fit (Table S5†), the second (minor) phase having the more closed-pore structure (smaller *a*-axis, larger *c*-axis). Upon subsequent heating steps, both phases show further progression along the anisotropic deformation pathway (*a*-axis decreasing, *c*-axis increasing) and the second phase increases in relative proportion. After heating at 433 K, all the material is converted into the more closed-pore phase and a single-phase fit to the pattern can be obtained.

**Adsorption of $CO_2$ by SHF-81.** Volumetric adsorption of $N_2$ gas by **SHF-81** at 77 K indicated minimal adsorption ($\approx 3$ cm$^3$ g$^{-1}$, Fig. S10†), whereas gravimetric measurements of $CO_2$ adsorption conducted at 273 K, 288 K and 298 K (Fig. 6a and Fig. S11†) indicated substantial adsorption (4.4 mmol g$^{-1}$ at 19 bar $CO_2$ ($p/p_0$ 0.52), 273 K; 3.6 mmol g$^{-1}$ at 19 bar $CO_2$ ($p/p_0$ 0.31), 298 K) and an isosteric enthalpy of adsorption, $\Delta H_{ads}$ (*i.e.* adsorption at zero surface coverage) of $-27.4$ kJ mol$^{-1}$ (Fig. S12†). One might infer substantial selectivity of adsorption of $CO_2$ over $N_2$ from these results, but further studies would be needed to quantify this. Our focus, however, has been to investigate whether $CO_2$ adsorption is a stimulus for anisotropic framework breathing that follows the reverse pathway observed for activation/desolvation. Thus, *in situ* synchrotron X-ray diffraction experiments were conducted at Diamond Light Source to study the effects of adsorption using PXRD at 298 K (0–50 bar $CO_2$, Fig. S13 and Table S6†) and SCXRD at 298 K (0–40 bar $CO_2$, Table S7†).

Both PXRD and SCXRD studies at 298 K show a small but rapid increase in unit cell volume at lower pressures ($p/p_0 < 0.1$, $p < 6$ bar $CO_2$), followed by a shallower increase until $p/p_0 \approx 0.6$ ($p \approx 37$ bar $CO_2$) and a further steep increase at $p/p_0 > 0.6$ (Fig. 6b and c), suggesting a potential gating of adsorption in the higher pressure range. The gravimetric adsorption data, which due to instrument limitations could not exceed a pressure of 20 bar, cover only the region of the diffraction studies at pressure below this apparent gating. The plots of *a*- *vs.* *c*-axis lengths show an increase in *a*-axis and decrease in *c*-axis length as $CO_2$ pressure is
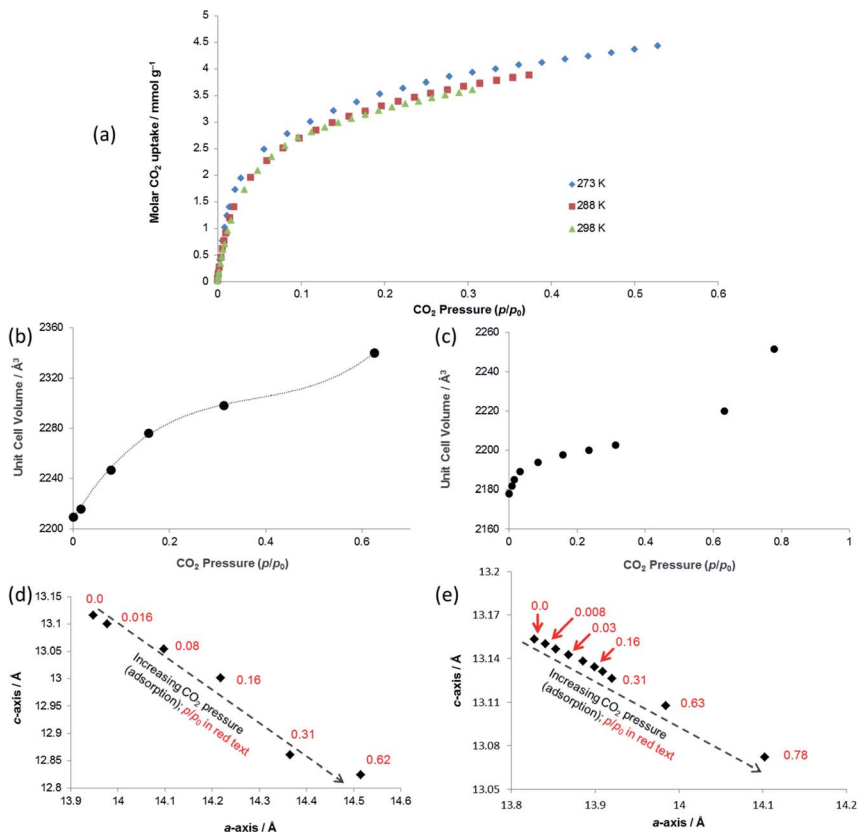
Fig. 6 (a) Gravimetric $CO_2$ adsorption isotherms at 273, 288 and 298 K for **SHF-81** (activated from **SHF-81-DMF**). Unit cell volume of **SHF-81** as a function of $CO_2$ pressure during (b) *in situ* SCXRD study at 298 K and (c) *in situ* PXRD study at 298 K. Lattice parameters for **SHF-81** as a function of increasing $CO_2$ pressure during (d) *in situ* SCXRD study at 298 K and (e) *in situ* PXRD study at 298 K. The dotted line in (b) is a guide to the eye, and illustrates the likely inflexion point slightly below $p/p_0$ 0.6. The arrows in (d) and (e) represent the direction of change for increasing $CO_2$ pressure (adsorption).

increased, consistent with the same framework breathing behaviour observed during the activation/desolvation of **SHF-81-DMF**, although with geometric changes in the opposite direction, *i.e.* negative linear expansion as $CO_2$ is adsorbed into the MOF pores. The range of changes in unit cell axis lengths and volume match reasonably well with those in the activation/desolvation study in the more closed-pore region of that study. Further studies (both adsorption and diffraction) at higher $CO_2$ pressures and/or lower temperatures (enabling higher $p/p_0$) would shed light on whether the geometries during the apparent adsorption gate are consistent with the observed step in observed geometries during activation/desolvation.

**Temperature-dependence of framework flexibility in SHF-81 and SHF-81-DMF.** A series of five variable-temperature X-ray diffraction experiments (*VT1–VT4*, SCXRD; *VT5*, PXRD) were conducted to provide further detail on the thermally induced flexibility of the framework. Study *VT1* comprised sequential full SCXRD data

collections using one crystal of **SHF-81-DMF** at 170, 140 and 100 K, including crystal structure refinements, and augments the data in Table 1. Other studies involved collection of only sufficient intensity data for accurate unit cell determination. Data were collected on two separate crystals of **SHF-81-DMF** at sequentially lower temperatures in studies *VT2* (160–85 K) and *VT3* (300–90 K). Data were collected on a crystal of activated/desolvated **SHF-81** at sequentially higher temperatures in study *VT4* (85–300 K). Study *VT5* comprised PXRD data for **SHF-81-DMF** in temperature steps from 300 K to 90 K and then, using the same steps, returning from 90 K to 300 K. Unit cell data for studies *VT1–VT5* are presented together with earlier data (Table 1) for **SHF-81-DMF** and **SHF-81** at different temperatures in Fig. 7. Data for the structurally closely related MOF QMOF-2, for which a prior study of linear NTE has been reported,[31] are included for comparison.

Both solvated **SHF-81-DMF** and activated/desolvated **SHF-81** exhibit linear NTE, wherein the *c*-axis (channel length) decreases with increasing temperature, whereas the *a*- and *b*-axes (channel width) increase. The geometric changes involved are analogous to those described in the earlier sections. Qualitatively similar thermally induced changes are observed for QMOF-2. It is notable, however, that despite the similarities in structure between **SHF-81/SHF-81-DMF** and QMOF-2, the latter has a shorter helical pitch along the channels (shorter *c*-axis) and displays a smaller range of dynamic motion.

### General discussion

The similarity in linear NTE behaviour of **SHF-81-DMF/SHF-81** and QMOF-2 is understandable given their shared framework topology, doubly interpenetrated networks and analogous $M(O_2CR)_4^{n-}$ network nodes and linker ligands ($NO_2BDC^{2-}$ and $BDC^{2-}$). Goodwin and co-workers have established that in quartz-like networks such as these the occurrence of linear NTE or PTE can be predicted geometrically
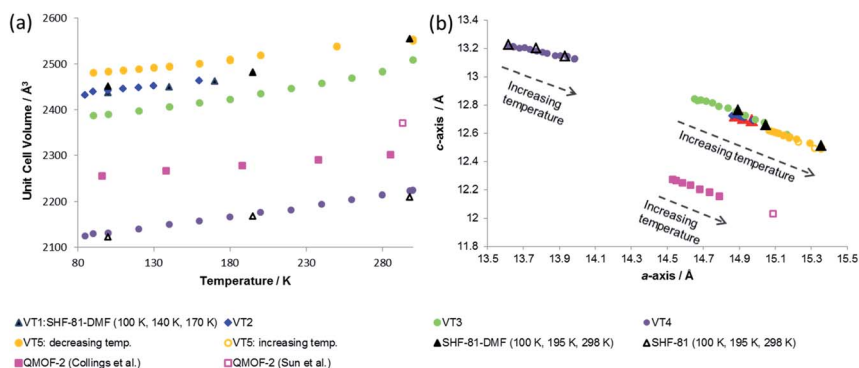


**Fig. 7** (a) Unit cell volume as a function of temperature and (b) lattice parameters during *in situ* SCXRD (*VT2, VT3*, **SHF-81-DMF**; *VT4*, **SHF-81**) and PXRD (*VT5*, **SHF-81-DMF**) studies. Data for full crystal structure determinations of **SHF-81-DMF** and **SHF-81** at different temperatures are included, as are data for the previously reported VT-NPD study[31] of desolvated QMOF-2 and single-crystal structure determination[45] of solvated QMOF-2 (note: the linear NTE behaviour of QMOF-2 was studied in the temperature range 12–285 K; data for the two studies conducted below 80 K are excluded from (a) for clarity of presentation, but studies over the full temperature range are included in (b)).

based on the $c/a$ ratio, $\rho$.[31] For $\rho < \rho_{critical}$ linear NTE occurs, whereas for $\rho > \rho_{critical}$ linear PTE should be expected. For these MOFs, $\rho_{critical} = 0.53$; $\rho = 0.82$–$0.85$ for QMOF-2, $\rho = 0.81$–$0.86$ for **SHF-81-DMF** and $\rho = 0.94$–$0.97$ for **SHF-81** over the temperature ranges studied, consistent with the linear NTE behaviour observed.

There is a marked difference in range of dynamic motion exhibited by the two MOFs, despite the frameworks being constructed with analogous ligands of the same length. The thermal expansion is of similar magnitude (Table 2) for both solvated **SHF-81-DMF** and desolvated **SHF-81**, and compares well with that of QMOF-2; there appears, however, to be a somewhat greater expansion for **SHF-81-DMF** in study *VT3*, which is likely to be a slightly desolvated crystal, based on the lattice parameters involved. The dynamic range resulting from activation/desolvation of **SHF-81-DMF** to **SHF-81** is, however, markedly greater (approx. four-fold) than that reported for QMOF-2 (Table 2). This could be a consequence of a number of factors, most obviously incomplete activation/desolvation for QMOF-2, as noted in the reported study.[31] There are a number of other differences between the two MOFs, notably the differences in metal–ligand bonding, wherein the $In^{III}$–O bonds in QMOF-2 are 0.05–0.2 Å shorter than the $Cd^{II}$–O bonds in **SHF-81-DMF**/ **SHF-81**,[46] which may lead to differences in how facile the carboxylate hinge-deformation integral to the breathing motion is. The dicarboxylate linker ligands also differ in the presence of the nitro substituent, which will have an electronic effect on metal–ligand bonding and a steric effect on channel dimensions. A final area of difference is the nature of the charge-balancing cation in the pore. In the case of **SHF-81-DMF**/**SHF-81**, SCXRD and $^1$H NMR evidence indicate that the MOF

**Table 2** Comparison of changes in lattice parameters for SHF-81-DMF, SHF-81 and QMOF-2 as a consequence of (i) increasing temperature and (ii) desolvation

Thermal

| MOF | $\Delta a$ (Å) | $\Delta c$ (Å) | Diffraction technique | Temperature range (increasing) | Notes |
|---|---|---|---|---|---|
| **SHF-81-DMF**[a] | 0.52 | −0.25 | SCXRD | 90–300 K | *VT3* |
| **SHF-81-DMF** | 0.29 | −0.13 | PXRD | 90–300 K | *VT5* |
| **SHF-81** | 0.34 | −0.083 | SCXRD | 90–300 K | *VT4* |
| QMOF-2[b] | 0.20 | −0.095 | NPD | 96–285[c] K | Ref. 31 |

Desolvation

| MOF | $\Delta a$ (Å) | $\Delta c$ (Å) | Diffraction technique | Temperature used for comparison | Notes |
|---|---|---|---|---|---|
| **SHF-81-DMF** | −1.42 | 0.63 | PXRD | 298 K | |
| **SHF-81-DMF** | −1.28 | 0.54 | SCXRD | 195 K | |
| **SHF-81-DMF** | −1.28 | 0.46 | SCXRD | 100 K | |
| QMOF-2 | −0.30 | 0.12 | NPD | 285–293[d] K | Partial desolvation[b] |

[a] Based on the range of unit cell dimensions it is most likely that this study is based on a partially desolvated crystal. [b] The authors note that D[In(BDC-d$_4$)$_2$] is not fully desolvated, as demonstrated by Rietveld fits.[31] [c] A range of temperatures that most closely matches the current studies is selected (full temperature range is 12–285 K). [d] Calculated based on differences between SCXRD unit cell for solvated H[In(BDC)$_2$] at 293 K (ref. 45) and PND unit cell for (partially) desolvated D[In(BDC-d$_4$)$_2$] at 285 K.[31]

retains two $Me_2NH_2^+$ cations per Cd(II) centre during the studies conducted. This situation is less clear, however, for QMOF-2. The original report provides a formula of $H[In(BDC)_2]\cdot nH_2O$,[45] although the synthetic route used will inevitably generate $Me_2NH_2^+$ cations. Closer inspection of the reported IR spectrum suggests the presence of $\nu(N–H)$ bands (at 3224 cm$^{-1}$) consistent with such cations, and TGA data include a mass loss at 220–250 °C consistent with loss of $Me_2NH$ from the cations, as also documented for **SHF-81** and other dimethylammonium-containing MOFs.[27] The fully deuterated QMOF-2 used in the thermal expansion study was prepared in an analogous manner to the original QMOF-2, and most likely has a composition of $(CD_3)_2ND_2[In(BDC\text{-}d_4)_2]\cdot n(DMF\text{-}d_7)\cdot m(D_2O)$. Upon activation, although the reported composition is $D[In(BDC\text{-}d_4)_2]\cdot guest$,[31] it is likely that $(CD_3)_2ND_2^+$ cations remain, given the activation procedure used.[47]

The differences in behaviour between the **SHF-81** and QMOF-2 systems suggest the possibility of tuning the dynamic behaviour by changing the nature of the substituent on the $BDC^{2-}$ ligand, through the use of mixed ligand MOFs and/or by changing the number and nature of the charge-balancing cations that reside in the MOF pores. The potential advantages and applications that many arise in the future from tuning anisotropic and negative expansion behaviour have been discussed by others. With that in mind, we note that a number of other analogues of these MOFs have been reported,[32,48] although this is a phase-rich area of MOF materials and to date, in our hands, many of these have proven challenging to isolate in phase-pure form on a practical scale.

Data from all diffraction studies are combined in Fig. 8 to convey the change in lattice parameters associated with the full range of breathing behaviour collectively probed by different stimuli. Notably, there are data points across the full range of lattice parameters 15.4 Å > $a$ > 13.6 Å and 12.5 Å < $c$ < 13.2 Å that lie approximately along a single line, suggesting the potential for a continuous breathing motion within this range of geometries with a negative correlation between $a$- and $c$-axis lengths. Activation/desolvation of **SHF-81-DMF** results in the largest changes, which span most of the full range of accessible dimensions. The $CO_2$ adsorption studies and thermal studies (90–300 K) give rise to changes of framework dimensions of similar magnitude, but smaller than those observed due to activation/desolvation. Although in principle higher pressures of $CO_2$ could be applied, the PXRD study reached $p/p_0$ of 0.8, which may suggest that $CO_2$ is not as effective an adsorbate for opening the MOF pores as the $DMF/H_2O$ solvent, consistent with the modest $CO_2$ adsorption enthalpy for **SHF-81**. Further investigations with a wider variety of adsorbates would be needed to describe the MOF performance more completely.

It is also apparent, particularly from the representation of the *in situ* studies in Fig. 8a, that what appear to be analogous studies are in fact conducted on samples in different initial states. Thus, thermal studies *VT2*, *VT3* and *VT5* clearly involve samples with different levels of partial desolvation, although all were ostensibly solvated **SHF-81-DMF**. The two *in situ* activation/desolvation studies, although starting at a similar point (slightly desolvated **SHF-81-DMF**), have endpoints with different geometries, the single-crystal sample being the more desolvated. This is most likely a consequence of the greater difficulty in solvent removal from the powder sample, as a consequence of its containment within a capillary. Study *VT4* and the two $CO_2$ adsorption studies have starting dimensions that suggest that these samples are a little more desolvated than the endpoints of the two
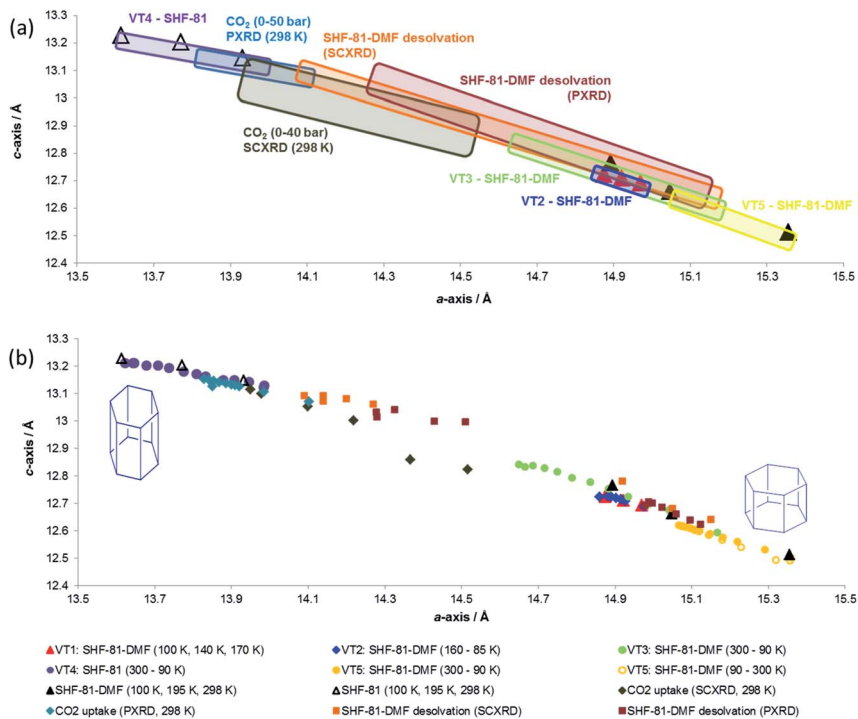
**Fig. 8** Combined plots showing change in lattice parameters as a function of different stimuli: activation/desolvation, $CO_2$ adsorption and temperature. (a) Each *in situ* diffraction study is represented by a rectangular box that encloses all data points associated with that study. Individual SCXRD studies at different temperatures (six **SHF-81-DMF**; three **SHF-81**) are denoted by triangular markers. (b) All individual data points associated with each study are shown. Colours and shapes of markers for individual data points are denoted in the legend.

desolvation studies. The difference in starting point between the two $CO_2$ adsorption studies (the PXRD sample is slightly more closed – smaller *a*-axis, larger *c*-axis) may be a factor in governing the smaller change in dimensions observed for the PXRD study than the SCXRD study. These observations indicate the challenges in clearly defining initial and final states in dynamic studies, such as this. The collective value of conducting a series of studies, using different stimuli and also different initial and final states, is also clearly demonstrated.

## Conclusions

The MOF $[Me_2NH_2]_2[Cd(NO_2BDC)_2]\cdot 2DMF\cdot 0.5H_2O$ (**SHF-81-DMF**) can be synthesised in good yield solvothermally by addition of a sub-stoichiometric amount (0.05 equiv.) of $[Me_2NH_2]Cl$. The MOF adopts a Dauphiné twinned α-quartz structure (trigonal, $P3_x21$, $x = 1, 2$) that deviates slightly from the higher symmetry β-quartz structure (hexagonal, $P6_x22$, $x = 2, 4$). Direct activation by heating to remove pore solvent reveals that the MOF is flexible and exhibits breathing behaviour. A series of *in situ* PXRD and SCXRD studies demonstrated that three

stimuli – (i) activation/desolvation, (ii) $CO_2$ adsorption and (iii) temperature – each led to breathing behaviour that is characterised by changes in the *a*-axis (*b*-axis) and *c*-axis dimensions that are opposite in sign, with magnitudes as large as $|\Delta a|$, $|\Delta b|$ < 1.8 Å and $|\Delta c|$ < 0.7 Å. The *a*- and *b*-axes quantify the width of pores, which run parallel to the *c*-axis and are defined by framework helices that increase in pitch as they narrow in diameter, and *vice versa*, during the reversible breathing behaviour. The thermal response of the MOF, either as solvated **SHF-81-DMF** or desolvated **SHF-81**, is described as linear negative thermal expansion. Adsorption of $CO_2$ by **SHF-81** can also be described as negative linear expansion, whereas activation/desolvation results in the reverse of the dynamic behaviour associated with adsorption. Comparison with the related β-quartz MOF $H[In(BDC)_2] \cdot$ guest (QMOF-2), which contains analogous building blocks and $M(O_2CR)_4^{n-}$ nodes and also exhibits linear NTE behaviour, suggests that there is an opportunity for tuning this behaviour based upon choice of metal ion and ligand potentially in a large family of related MOFs. We are actively exploring this potential.

## Conflicts of interest

There are no conflicts of interest.

## Acknowledgements

## References

1 D. M. D'Alessandro, B. Smit and J. R. Long, *Angew. Chem., Int. Ed.*, 2010, **49**, 6058–6082.

2 L. J. Murray, M. Dincă and J. R. Long, *Chem. Soc. Rev.*, 2009, **38**, 1294–1314.

3 M. P. Suh, H. J. Park, T. K. Prasad and D. Lim, *Chem. Rev.*, 2012, **112**, 782–835.

4 A. Corma, H. Garcia and F. X. Llabres i Xamena, *Chem. Rev.*, 2010, **110**, 4606–4655.

5 Y. Liu, W. Xuan and Y. Cui, *Adv. Mater.*, 2010, **22**, 4112–4135.

6 J. Liu, L. Chen, H. Cui, J. Zhang, L. Zhang and C.-Y. Su, *Chem. Soc. Rev.*, 2014, **43**, 6011–6061.

7 Y. Zhao, Z. Song, X. Li, Q. Sun, N. Cheng, S. Lawes and X. Sun, *Energy Storage Materials*, 2016, **2**, 35–62.

8 L. E. Kreno, K. Leong, O. K. Farha, M. Allendorf, R. P. Van Duyne and J. T. Hupp, *Chem. Rev.*, 2012, **112**, 1105–1125.

9 E. Barea, C. Montoro and J. A. R. Navarro, *Chem. Soc. Rev.*, 2014, **43**, 5419–5430.

10 S. Kitagawa and K. Uemura, *Chem. Soc. Rev.*, 2005, **34**, 109–119.

11 S. Horike, S. Shimomura and S. Kitagawa, *Nat. Chem.*, 2009, **1**, 695–704.

12 G. Férey and C. Serre, *Chem. Soc. Rev.*, 2009, **38**, 1380–1399.

13 C. R. Murdock, B. C. Hughes, Z. Lu and D. M. Jenkins, *Coord. Chem. Rev.*, 2014, **258–259**, 119–136.

14 A. Schneemann, V. Bon, I. Schwedler, I. Senkovska, S. Kaskel and R. A. Fischer, *Chem. Soc. Rev.*, 2014, **43**, 6062–6096.

15 G. Fraux and F.-X. Coudert, *Chem. Commun.*, 2017, **53**, 7211–7221.

16 I. E. Collings and A. L. Goodwin, *J. Appl. Phys.*, 2019, **126**, 181101.

17 L. Li, R.-B. Lin, R. Krishna, X. Wang, B. Li, H. Wu, J. Li, W. Zhou and B. Chen, *J. Am. Chem. Soc.*, 2017, **139**, 7733–7736.

18 S. Yuan, L. Zou, H. Li, Y.-P. Chen, J. Qin, Q. Zhang, W. Lu, M. B. Hall and H.-C. Zhou, *Angew. Chem., Int. Ed.*, 2016, **55**, 10776–10780.

19 X.-Y. Dong, H.-L. Huang, J.-Y. Wang, H.-Y. Li and S.-Q. Zang, *Chem. Mater.*, 2018, **30**, 2160–2167.

20 P. G. Yot, L. Vanduyfhuys, E. Alvarez, J. Rodriguez, J.-P. Itié, P. Fabry, N. Guillou, T. Devic, I. Beurroies and P. L. Llewellyn, *Chem. Sci.*, 2016, **7**, 446–450.

21 J. Troyano, A. Carné-Sánchez, J. Pérez-Carvajal, L. León-Reina, I. Imaz, A. Cabeza and D. Maspoch, *Angew. Chem., Int. Ed.*, 2018, **57**, 15420–15424.

22 (*a*) C. Serre, F. Millange, C. Thouvenot, M. Noguès, G. Marsolier, D. Louër and G. Férey, *J. Am. Chem. Soc.*, 2002, **124**, 13519–13526; (*b*) P. L. Llewellyn, P. Horcajada, G. Maurin, T. Devic, N. Rosenbach, S. Bourrelly, C. Serre, D. Vincent, S. Loera-Serna, Y. Filinchuk and G. Férey, *J. Am. Chem. Soc.*, 2009, **131**, 13002–13008.

23 (*a*) Z. Wang and S. M. Cohen, *J. Am. Chem. Soc.*, 2009, **131**, 16675–16677; (*b*) J. S. Grosch and F. Paesani, *J. Am. Chem. Soc.*, 2012, **134**, 4207–4215; (*c*) S. Henke, A. Schneemann, A. Wütscher and R. A. Fischer, *J. Am. Chem. Soc.*, 2012, **134**, 9464–9474.

24 (*a*) H. J. Choi, M. Dincă and J. R. Long, *J. Am. Chem. Soc.*, 2008, **130**, 7848–7850; (*b*) J. A. Mason, J. Oktawiec, M. K. Taylor, M. R. Hudson, J. Rodriguez, J. E. Bachman, M. I. Gonzalez, A. Cervellino, A. Guagliardi, C. M. Brown, P. L. Llewellyn, N. Masciocchi and J. R. Long, *Nature*, 2015, **527**, 357–361; (*c*) M. K. Taylor, T. Runčevski, J. Oktawiec, M. I. Gonzalez, R. L. Siegelman, J. A. Mason, J. Ye, C. M. Brown and J. R. Long, *J. Am. Chem. Soc.*, 2016, **138**, 15019–15026; (*d*) M. K. Taylor, T. Runčevski, J. Oktawiec, J. E. Bachman, R. L. Siegelman, H. Jiang, J. A. Mason, J. D. Tarver and J. R. Long, *J. Am. Chem. Soc.*, 2018, **140**, 10324–10331.

25 (*a*) A. P. Katsoulidis, K. S. Park, D. Antypov, C. Martí-Gastaldo, G. J. Miller, J. E. Warren, C. M. Robertson, F. Blanc, G. R. Darling, N. G. Berry, J. A. Purton, D. J. Adams and M. J. Rosseinsky, *Angew. Chem., Int. Ed.*, 2014, **53**, 193–198; (*b*) A. P. Katsoulidis, D. Antypov, G. F. S. Whitehead, E. J. Carrington, D. J. Adams, N. G. Berry, G. R. Darling, M. S. Dyer and M. J. Rosseinsky, *Nature*, 2019, **565**, 213–217; (*c*) S. Krause, V. Bon, I. Senkovska, U. Stoeck, D. Wallacher, D. M. Többens, S. Zander, R. S. Pillai, G. Maurin, F.-X. Coudert and S. Kaskel, *Nature*, 2016, **532**, 348–352.

26 (*a*) C. S. C. Mellot-Draznieks, S. Surblé, N. Audebrand, Y. Filinchuk and G. Férey, *Science*, 2007, **315**, 1828–1831; (*b*) P. Horcajada, F. Salles, S. Wuttke, T. Devic, D. Heurtaux, G. Maurin, A. Vimont, M. Daturi, O. David, E. Magnier, N. Stock, Y. Filinchuk, D. Popov, C. Riekel, G. Férey and C. Serre, *J. Am. Chem. Soc.*, 2011, **133**, 17839–17847.

27 E. J. Carrington, C. A. McAnally, A. J. Fletcher, S. P. Thompson, M. Warren and L. Brammer, *Nat. Chem.*, 2017, **9**, 882–887.

28 A. L. Goodwin, M. Calleja, M. J. Conterio, M. T. Dove, J. S. O. Evans, D. A. Keen, L. Peters and M. G. Tucker, *Science*, 2008, **319**, 794–797.

29 (a) R. Baughman, S. Stafstrom, C. Cui and S. Dantas, *Science*, 1998, **279**, 1522–1524; (b) A. B. Cairns, J. Catafesta, C. Levelut, J. Rouquette, A. van der Lee, L. Peters, A. L. Thompson, V. Dmitriev, J. Haines and A. L. Goodwin, *Nat. Mater.*, 2013, **12**, 212–216; (c) A. B. Cairns and A. L. Goodwin, *Phys. Chem. Chem. Phys.*, 2015, **17**, 20449–20465.

30 J. N. Grima, R. Gatt, V. Zammit, J. J. Williams, K. E. Evans, A. Alderson and R. I. Walton, *J. Appl. Phys.*, 2007, **101**, 086102.

31 I. E. Collings, M. G. Tucker, D. A. Keen and A. L. Goodwin, *CrystEngComm*, 2014, **16**, 3498–3506.

32 X.-F. Wang, Y.-B. Zhang and Y.-Y. Lin, *CrystEngComm*, 2013, **15**, 3470–3477.

33 S. P. Thompson, J. E. Parker, J. Potter, T. P. Hill, A. Birt, T. M. Cobb, F. Yuan and C. C. Tang, *Rev. Sci. Instrum.*, 2009, **80**, 075107.

34 S. P. Thompson, J. E. Parker, J. Marchal, J. Potter, A. Birt, F. Yuan, R. D. Fearn, A. R. Lennie, S. R. Street and C. C. Tang, *J. Synchrotron Radiat.*, 2011, **18**, 637–648.

35 G. S. Pawley, *J. Appl. Crystallogr.*, 1981, **14**, 357–361.

36 (a) A. A. Coelho, *TOPAS Academic Version 4.1*, 2007, see http//www.topas-academic.net; (b) A. A. Coelho, *J. Appl. Crystallogr.*, 2018, **51**, 210–218; (c) A. A. Coelho, J. Evans, I. Evans, A. Kern and S. Parsons, *Powder Diffr.*, 2011, **26**, S22–S25.

37 *APEX3*, Bruker AXS Inc., Madison, Wisconsin, USA, 2016.

38 (a) SADADS, empirical absorption correction program, based on the method of Blessing[38b] L. Krause, R. Herbst-Irmer, G. M. Sheldrick and D. Stalke, *J. Appl. Crystallogr.*, 2015, **48**, 3–10 ; (b) R. H. Blessing, *Acta Crystallogr., Sect. A: Found. Crystallogr.*, 1995, **51**, 33–38.

39 H. Nowell, S. A. Barnett, K. E. Christensen, S. J. Teat and D. R. Allan, *J. Synchrotron Radiat.*, 2012, **19**, 435–441.

40 *CrysAlis^{PRO}*, Rigaku Oxford Diffraction.

41 G. M. Sheldrick, *Acta Crystallogr., Sect. C: Struct. Chem.*, 2015, **71**, 3–8.

42 O. V. Dolomanov, L. J. Bourhis, R. J. Gildea, J. A. K. Howard and H. Puschmann, *J. Appl. Crystallogr.*, 2009, **42**, 339–341.

43 A. L. Spek, *Acta Crystallogr., Sect. C: Struct. Chem.*, 2015, **71**, 9–18.

44 (a) A. F. Wright and M. S. Hehmann, *J. Solid State Chem.*, 1981, **36**, 371–380; (b) K. Kihara, *Eur. J. Mineral.*, 1990, **2**, 63–77; (c) J. Van Landuyt, G. Van Tendeloo, S. Amelinckx and M. B. Walker, *Phys. Rev. B: Condens. Matter Mater. Phys.*, 1985, **31**, 2986–2992.

45 J. Sun, L. Weng, Y. Zhou, J. Chen, Z. Chen, Z. Liu and D. Zhao, *Angew. Chem., Int. Ed.*, 2002, **41**, 4471–4473.

46 **SHF-81-DMF:** Cd–O bond lengths 2.314–2.494 Å; QMOF-2 (ref. 45): In–O bond lengths 2.267–2.282 Å.

47 (a) Kang and coworkers report[47b] that $Me_2NH_2^+$ cations lose $Me_2NH$ at approximately 250–300 °C in as-synthesised QMOF-2 (TGA measurements), but also report that $Me_2NH$ loss occurs by heating at 60 °C under vacuum for an unspecified time period, after first exchanging pore-solvent with $CH_2Cl_2$ (by an unspecified procedure); (b) W. Ji, H. Hu, W. Zhang, H. Huang, X. He, X. Han, F. Zhao, Y. Liu and Z. Kang, *Dalton Trans.*, 2013, **42**, 10690–10693.

48 M. Krüger, M. Albat, A. K. Inge and N. Stock, *CrystEngComm*, 2017, **19**, 4622–4628.